Spatial Expression of Long Non-Coding RNAs in Human Brains of Alzheimer's Disease

Bernard Ng[1, #], Denis R. Avey[1, 5, #], Katia de Paiva Lopes[1], Masashi Fujita[2], Ricardo A. Vialle[1], Himanshu Vyas[1], Nicola A. Kearns[1, 5], Shinya Tasaki[1], Artemis Iatrou[1,3], Sashini De Tissera[1], Tien-Hao Chang[1], Jishu Xu[1], Chunjiang Yu[1], Faraz Sultan[1], Vilas Menon[2], Chris Gaiteri[1,4], Philip L. De Jager[2], David A. Bennett[1, 5], Yanling Wang[1, 5, *]

1. Rush Alzheimer's Disease Center, Rush University Medical Center, Chicago, IL, 60612, USA
2. Center for Translational and Computational Neuroimmunology, Department of Neurology, Columbia University Irving Medical Center, New York, NY, USA
3. Current affiliation: Department of Psychiatry, McLean Hospital, Harvard Medical School, Belmont, MA, 02478, USA
4. Department of Psychiatry, Upstate Medical University, Syracuse, NY, 13210, USA
5. Department of Neurological Sciences, Rush University Medical Center, Chicago, IL, 60612, USA

[#]Contributed equally

*Correspondence to yanling_wang@rush.edu

Abstract

Long non-coding RNAs (lncRNAs) are critical regulators of physiological and pathological processes, with their dysregulation increasingly implicated in aging and Alzheimer's disease (AD). Using spatial transcriptomics, we analyzed 78 postmortem brain sections from 21 ROSMAP participants to map the spatial expression of lncRNAs in the dorsolateral prefrontal cortex of aged human brains. Compared to mRNAs, lncRNAs exhibited greater subregion-specific expression, with enrichment in antisense and lincRNA biotypes. Network analysis identified 193 gene modules across eight subregions, including lncRNA-enriched modules involved in critical biological processes. We also identified AD differentially expressed (DE) lncRNAs, which showed greater subregion specificity than AD DE mRNAs. Gene set enrichment analysis highlighted the involvement of these AD DE lncRNAs in epigenetic regulation and chromatin remodeling, including enrichment for HDAC target genes such as *OIP5-AS1*. Statistical modeling suggested that interactions between *OIP5-AS1* and HDAC proteins, particularly HDAC11, were associated with tau tangles in excitatory neurons and plaque burden in microglia. This study provides a comprehensive resource of lncRNA spatial expression in the aged human brain and uncovers potential functional roles of lncRNAs in AD pathogenesis.

Introduction

One of the most remarkable discoveries of the 21st century is that a significant portion of the genome is transcribed into RNAs with little or no protein-coding potential[1,2]. While approximately 90% of the human genome is transcribed, only about 2% is annotated as protein-coding genes. This paradigm-shifting discovery has spurred extensive research into the regulatory roles of non-coding RNAs (ncRNAs) in gene expression[2,3], redefining our understanding of the genome and challenging the traditional view that only protein-coding genes are functionally significant.

Among ncRNAs, long non-coding RNAs (lncRNAs) represent a prominent class of transcripts longer than 200 nucleotides, predominantly transcribed by RNA Polymerase II. LncRNAs regulate gene expression through diverse mechanisms, including epigenetic modification, chromatin remodeling, and post-transcriptional processes[4,5]. Compared to coding RNAs, lncRNAs exhibit greater tissue and cell-type specificity[6,7] and are particularly abundant in the human brain, where they play critical roles in neuronal differentiation, synaptogenesis, and neuroplasticity[1,8]. Dysregulated lncRNA expression has been implicated in numerous neurological disorders, including Alzheimer's disease (AD). In AD, aberrant lncRNA expression has been linked to key pathological processes, such as amyloid-beta metabolism, tau pathology, neuroinflammation, and neuronal death[9–13]. However, the spatial and cellular contexts in which lncRNAs might influence AD-related processes remain largely unexplored.

In this study, we present the spatial expression profiles of lncRNAs in the dorsolateral prefrontal cortex (DLPFC) of 21 participants from Religious Orders Study and Memory and Aging Project (ROSMAP). We identify subregion-specific lncRNAs and examine their overlap with cell-type-specific lncRNAs. Additionally, we map lncRNAs and mRNAs that are differentially expressed (DE) in AD across distinct subregions, comparing our spatial transcriptomics (ST) results with findings from bulk RNA-seq and single-nucleus RNA-seq (snRNA-seq) analyses. Finally, we infer potential interactions between *OIP5-AS1* and histone deacetylase (HDAC) proteins, particularly HDAC11, providing new insights into the functional roles of lncRNAs in AD pathogenesis.

Results

Spatial expression of lncRNAs in aged human brains

Using our recently acquired ST data[14], we analyzed lncRNA expression from 78 DLPFC sections of 21 female individuals (AD = 13; no cognitive impairment (NCI) = 8). In total, we detected 7,634 lncRNAs and 16,769 protein-coding mRNAs across 8 spatial spot clusters corresponding to subregions: layer 1 (L1), layers 2–3 (L2–3), layers 3–5 (L3–5), layer 5 (L5), layer 6 (L6), white matter (WM), meninges, and

64 blood vessels (Fig. 1A). Consistent with prior studies[6,7], lncRNAs exhibited lower expression levels than
65 mRNAs (Fig. 1B), with most lncRNAs detected in fewer than 0.01% of ST spots (Fig. 1C). For
66 downstream analysis, we retained 1,578 lncRNAs and 13,808 mRNAs with adequate expression
67 (counts per million [CPM] >1 in >80% of brain sections). Among the detected lncRNAs, the most
68 prevalent biotypes were lincRNAs and antisense transcripts (Fig. 1D). Notably, lncRNAs demonstrated
69 greater subregion specificity, with only 39.9% of lncRNAs detected across all eight subregions, compared to
70 89.3% of mRNAs (Fig. 1E).

71 By contrasting the expression of spatial spots in one subregion against all others, we identified 79
72 subregion-specific lncRNAs (Fig. 2A–2C; Table S1). To investigate whether subregion-specific
73 lncRNAs also exhibit cell-type specificity, we cross-referenced a published snRNA-seq dataset derived
74 from the DLPFC of 424 ROSMAP participants[15]. While we observed limited overlap between subregion-
75 specific and cell-type-specific lncRNAs (Fig. 2D; Table S1), some exceptions emerged. For example,
76 *AL031056.1* was enriched in L1 (Fig. 2A) and astrocytes (Fig. 2D), *LINC00507* in L2–3 (Fig. 2A) and
77 excitatory neurons (Fig. 2D), *AC021613.1* in L6 (Fig. 2A, 2C) and excitatory neurons (Fig. 2D), and
78 *AC092958.1*, *TYMSOS*, and *LINC00844* in WM (Fig. 2A, 2B) and oligodendrocytes (Fig. 2C, 2D).
79 However, the majority of subregion-specific lncRNAs were not confined to specific cell types (Fig. 2D).

80 We next examined whether cell-type-specific lncRNAs exhibited subregion specificity. Although general
81 trends emerged, such as astrocyte-specific lncRNAs being more abundant in L1, excitatory/inhibitory
82 neuron-specific lncRNAs in cortical layers, and oligodendrocyte-specific lncRNAs in WM, most cell-
83 type-specific lncRNAs were expressed across multiple subregions (Fig. 2E; Table S1). These
84 observations likely reflect the heterogeneity of cell types within each subregion and the shared
85 developmental origins of cell types that span cortical layers. Nonetheless, the identification of both
86 subregion-specific and cell-type-specific lncRNAs suggests that some lncRNAs function within precise
87 spatial regions to support localized processes, while others serve the specific needs of individual cell
88 types.

89 **lncRNA-enriched gene modules in aged human brains**

90 To investigate the molecular systems within each subregion, we derived a pseudo-bulk matrix for each
91 subregion and performed co-expression network analysis using the Speakeasy algorithm[16] (Fig. 3A).
92 Both lncRNAs and mRNAs were included to capture their potential interactions across biological
93 processes. This analysis generated 193 modules, each containing at least 30 genes (Table S2). Module
94 preservation analysis revealed that cortical layer modules were more preserved than those derived
95 from WM, blood vessels, and meninges (Fig. 3B; Table S3). Within individual subregions, 15–60% of

96 the modules were lncRNA-enriched (Fig. 3C). For example, the L2-3_m14 module, comprising 1,261
97 genes, was enriched with 210 lncRNAs (Bonferroni $p < 0.05$), including 4 reported AD-differential
98 lncRNAs[9,10,17], 3 AD-GWAS genes[18], and 23 AD-differential lncRNA genes based on our ST analysis
99 (Fig. 3D; Tables S2, S6). Gene Ontology (GO) analysis revealed that L2-3_m14 was enriched for
100 biological processes, such as metabolism, cell cycle regulation, ncRNA processing, and positive
101 regulation of telomerase (Fig. 3E, Table S4). Similarly, the WM_m11 module, containing 1,148 genes,
102 was enriched with 156 lncRNAs (Bonferroni $p < 0.05$), including 2 previously reported AD-differential
103 lncRNAs[9,10,17], 4 AD-GWAS genes[18], and 29 AD-differential lncRNAs based on our ST analysis (Fig.
104 3F; Tables S2, S6). GO analysis indicated that WM_m11 was associated with processes such as
105 carbohydrate derivative metabolism, lipid metabolic modification, and nervous system development
106 (Fig. 3G, Table S4). In addition, we conducted module-trait association analysis and detected a small
107 fraction of modules associated with AD traits (nominal $p < 0.05$), including lncRNA-enriched modules
108 (Table S5).

109 **AD DE lncRNAs and cross-modality comparisons**

110 To identify DE lncRNAs in AD compared to NCI, we aggregated spot-level expression values within
111 each brain section to generate a pseudo-bulk matrix for each subregion. These estimates were
112 normalized using TMM-voom[19], and linear mixed models (LMM) were applied to contrast AD against
113 NCI while adjusting for age, RNA Integrity Number (RIN), postmortem interval (PMI). Batch effects were
114 included as fixed effects, and within-subject correlations were modeled as random effects. After
115 applying false discovery rate (FDR) correction across genes and subregions, we identified 275 AD DE
116 lncRNAs (Table S6). Notably, a greater proportion of these lncRNAs exhibited negative associations
117 with AD compared to mRNAs (Fig. 4A, 4B). Biotype analysis revealed enrichment of bidirectional
118 promoter lncRNAs in L3–5 and lincRNAs in L6 and WM (Fig. 4C).

119 Next, we compared our ST-derived AD DE lncRNAs and mRNAs with those identified from bulk RNA-
120 seq data of the DLPFC in 1,049 individuals[20] (Table S6). Although the overlap of AD DE genes between
121 ST and bulk RNA-seq was modest (Fig. 4D), t-values for all lncRNAs and mRNAs exhibited moderate
122 correlations between the two modalities ($R = 0.3$ for lncRNAs; $R = 0.39$ for mRNAs; Fig. 4E).
123 Concordant findings included several downregulated lncRNAs, such as *LY86-AS1*, *FAM106A*,
124 *LINC01007*, and *MIR7-3HG*, as well as upregulated lncRNAs, including *NEAT1*, *LINC00632*, *FGD5-*
125 *AS1*, and *LINC01094* in AD brains (Fig. 4E).

126 Consistent with our ST findings, snRNA-seq analysis also showed that DE lncRNAs were more
127 frequently negatively associated with AD than DE mRNAs (Fig. S1A– S1B; Table S6). Additionally, AD

128 DE lncRNAs were enriched for lincRNAs, particularly in inhibitory neurons and oligodendrocyte
129 precursor cells (OPCs) (Fig. S1C). These DE lncRNAs also displayed greater cell-type specificity in
130 oligodendrocytes, inhibitory neurons, and excitatory neurons compared to DE mRNAs (Fig. S1D).
131 However, overlaps between subregion-specific and cell-type-specific AD DE lncRNAs were minimal
132 (Fig. S1E).

133 Pairwise t-value correlations revealed moderate alignment between L3–5 and inhibitory neurons, as
134 well as between blood vessels and microglia/oligodendrocytes (Fig. S1F). While a larger proportion of
135 DE mRNAs were shared across subregions and cell types (Fig. S1E), t-value correlations between
136 subregions and cell types remained weak (Fig. S1G), likely reflecting differences in resolution and
137 sensitivity between ST and snRNA-seq platforms.

138 **Spatial expression of AD DE lncRNAs and their functional implications**

139 When comparing AD DE lncRNAs and mRNAs, we found that DE lncRNAs were generally more
140 subregion-specific than DE mRNAs, with 115 of 275 DE lncRNAs showing subregion-specific
141 differential expression in the cortex (Fig. 5A; Table S6). A higher proportion of DE lncRNAs were
142 specifically expressed in the meninges, L2–3, L3–5, L5, and L6 (Fig. 5A). Notably, these subregion-
143 specific DE lncRNAs, regardless of whether they were up- or downregulated, did not appear to be cell-
144 type-specific (Fig. 5B). The remaining 160 of 275 AD DE lncRNAs were differentially expressed across
145 multiple subregions, with the majority (~93%) being novel lncRNAs (Fig. 5C). Among the 11 DE
146 lncRNAs that were previously reported[9,10,17], 8 were also-replicated in bulk RNA-seq datasets (Fig. 5C,
147 bottom row; Table S6).

148 Some AD DE lncRNAs displayed high expression in one subregion but showed predominant AD effects
149 in other subregions. For example, *LINC00844* was highly expressed in WM/oligodendrocytes (Fig. 2A,
150 2B) but exhibited its strongest AD effects in L2-3 (Fig. 5B). Similarly, *LINC00507* showed high
151 expression in L2-3 but demonstrated predominant AD effects in L3-6 (Fig. 5C). On the other hand, the
152 X-inactive-specific transcript (*XIST*), which was broadly expressed across all subregions (Fig. 2A, Fig.
153 5D), showed its AD effects primarily in L1 and L2–3 (Fig. 5C, 5E). The detection of DE *XIST* prompted
154 an investigation into other X-linked genes, revealing that *MECP2* was upregulated in L5, while *PGK1*
155 was downregulated in L1, L2–3, and blood vessels in AD brains (Fig. 5E).

156 To further explore functional implications, we applied gene set enrichment analysis (GSEA) on t-values
157 for all genes across subregions, focusing on gene sets containing AD DE lncRNAs. This analysis
158 revealed enrichment for processes such as cell motility (*MALAT1*, *SPATA13*), apoptosis (*ARMCX5-*
159 *GPRASP2*), chromatin organization (*XIST*, *KCNQ1OT1*), and regulation of defense responses

(*NEAT1*) (Fig. 5F; Table S7–8). Notably, we also observed enrichment for HDAC targets, which included three AD DE lncRNAs (*FGD5-AS1*, *NNT-AS1*, *OIP5-AS1*) (Fig. 5F; Table S8). Consistent with this finding, several HDACs (*HDAC1*, *HDAC3*, *HDAC6*, *HDAC7*, and *HDAC10*) were differentially expressed in one or more subregions of AD brains (Fig. 5G). These results support growing evidence implicating HDACs in AD pathogenesis[21,22] and suggest a potential functional link between specific lncRNAs and HDAC activity.

Inferred interaction between *OIP5-AS1* and HDAC11 is associated with AD traits

HDAC inhibition has been extensively studied as a potential therapeutic approach for AD[21,23–25]. However, the lack of selectivity in current HDAC inhibitors often results in unintended off-target effects[26,27]. Our GSEA identified specific lncRNAs, including *FGD5-AS1*, *NNT-AS1*, and *OIP5-AS1*, that may interact with HDACs, suggesting a potential strategy to selectively modulate HDAC activity in AD treatment. Among these lncRNAs, *OIP5-AS1* (Cyrano) has been implicated in a wide range of biological processes, including development[28–30], cancer progression[31–34], and cerebral ischemia-reperfusion injury[35].

To validate *OIP5-AS1* expression, we performed RNAscope and immunohistochemistry (IHC) on postmortem DLPFC sections from ROSMAP participants (n=8). Consistent with our ST findings, *OIP5-AS1* was broadly expressed across cortical layers, particularly in L2-3 (Fig. S2A, S2B). At the cellular level, *OIP5-AS1* expression was detected in MAP2+ neurons and IBA1+ microglia (Fig. S2A, S2C).

These observations prompted further investigation into whether genetic variation influences *OIP5-AS1* expression and whether its interactions with HDACs are associated with clinical and pathological AD traits. Using the published snRNA-seq dataset[15], we first curated expression quantitative trait loci (eQTL) statistics of SNPs within 1 Mb of *OIP5-AS1's* transcription start site (TSS) across six major brain cell types. Multivariate fine-mapping[36] identified rs1655558 as a potential causal variant influencing *OIP5-AS1* expression in multiple cell types, including excitatory neurons, astrocytes, and oligodendrocytes (Fig. 6A). We then examined the interaction between *OIP5-AS1* expression in six cell types and HDAC protein abundance in the DLPFC using a published proteomics dataset [37]. These interactions were tested for associations with AD-related traits: cognitive decline, neuritic plaques, and tau tangles (Fig. 6B). Significant interaction effects were declared at an α of 0.05, corrected for the number of cell types and HDACs tested. Our analysis revealed that interactions between *OIP5-AS1* and HDACs were more strongly associated with tau tangles and neuritic plaques than with cognitive decline (Fig. 6C, left). Notably, some interaction effects exhibited p-values an order of magnitude lower than the main effects of HDACs alone (circled dots in Fig. 6D, 6G), suggesting that *OIP5-AS1* plays a

critical modulatory role in HDAC-mediated AD pathology. Comparable trends were observed when using HDAC mRNA expression instead of protein abundance, although interaction effects were weaker (Fig. 6C, right; Fig. S3), indicating that *OIP5-AS1* primarily interacts with HDAC proteins rather than their transcripts in influencing AD pathophysiology.

The interaction between *OIP5-AS1* and HDAC11 was particularly striking. In excitatory neurons, this interaction was associated with tau pathology (Fig. 6D), with the strongest effects observed in the hippocampus and medial temporal lobe (Fig. 6E). In microglia, the interaction was associated with neuritic plaques (Fig. 6G), with similarly pronounced effects in the same brain regions (Fig. 6H). Stratifying 424 ROSMAP participants[15] into tertiles based on *OIP5-AS1* expression levels in excitatory neurons or microglia revealed that HDAC11 protein abundance was positively associated with tau tangles only when *OIP5-AS1* expression was high in excitatory neurons (Fig. 6F). Conversely, HDAC11 protein abundance was positively associated with plaques only when *OIP5-AS1* expression was low in microglia (Fig. 6I). These findings suggest that *OIP5-AS1* interacts with HDACs, particularly HDAC11, in a cell-type-specific manner, modulating their effects on AD pathology.

Discussion

Recent advancements in sequencing technologies have revealed that a significant portion of the mammalian genome is transcribed into lncRNAs[1]. While the brain expresses more tissue-specific lncRNAs than most other tissues[38,39], their spatial and cellular contexts in the human brain remain poorly understood. In this study, we mapped the spatial expression of lncRNAs in DLPFC of aged human brains and found that lncRNAs exhibit lower overall expression levels and more restricted spatial patterns compared to mRNAs (Fig. 1). Using a published snRNA-seq dataset[15], we compared subregion- and cell-type-specific lncRNAs and observed limited overlap, with some alignment between white matter and oligodendrocytes (Fig. 2). Additionally, we identified numerous subregion-specific lncRNA-enriched gene modules associated with diverse biological processes (Fig. 3), suggesting that lncRNAs may influence brain function by interacting with mRNAs within shared molecular systems.

Out of 275 DE lncRNAs, 11 DE lncRNAs were previously reported in AD studies (Fig. 5C). For example, we observed higher expression of *MALAT1*, *NEAT1*, *BACE1-AS*, and *BDNF-AS* in AD individuals, consistent with their known roles in AD pathogenesis. *BACE1-AS* promotes amyloid production[40–42], while *BDNF-AS* modulates synaptic plasticity through interactions with its mRNA counterpart[43–45]. *MALAT1*, a major organizer of nuclear speckles, suppresses neuronal apoptosis and inflammation by modulating *miR-125b*[46,47]. Similarly, *NEAT1* regulates tau phosphorylation and Aβ metabolism through interactions with *miR-124*, *miR-107*, and histone acetyltransferases[48,49]. In addition, we identified

224 emerging immune- and aging-associated lncRNAs, such as *LY86-AS1*[50], *FAM106A*[51], and *MIR7-*
225 *3HG*[52].

226 Increased *XIST* levels have been previously reported in the brains of female AD patients and linked to
227 X Chromosome Interaction (XCI), a process contributing to female-specific vulnerability in AD[53,54]. We
228 detected an upregulation of *XIST* in AD, primarily in the upper cortical layers (Fig. 5C-5E). Since our
229 study included only females, this upregulation suggests disrupted XCI in AD, potentially leading to
230 silencing of some X-linked genes and/or overexpression of escapee genes. Consistently, we observed
231 altered expression of X-linked genes, such as *MECP2*, *PGK1*, *MAOA*, and *HPRT1* (Fig. 5D, 5E; Table
232 S6), which are critical for neuronal function, epigenetic regulation, and cellular metabolism[55–59].

233 Gene set enrichment analysis revealed that AD DE lncRNAs are involved in diverse regulatory
234 processes, including epigenetic regulation, chromatin remodeling, and RNA metabolism. One key
235 finding was the enrichment of HDAC target genes, including *FGD5-AS1*, *NNT-AS1*, and *OIP5-AS1*.
236 Among these, *OIP5-AS1* stands out for its diverse regulatory roles[60]. *OIP5-AS1* has been shown to
237 regulate cell proliferation, apoptosis, migration, and invasion in cancer through miRNA sponging and
238 interactions with chromatin modifiers, such as HDACs[31–34,61]. In the brain, *OIP5-AS1* is upregulated in
239 M2 microglia-derived exosomes, where it inhibits neuronal pyroptosis via ubiquitination of its binding
240 protein TXNIP[35]. Additionally, it acts as a central player in a non-coding RNA network by degrading
241 mature *miR-7*, thereby modulating neuronal activity[62].

242 Using statistical modeling, we inferred that the interactions between *OIP5-AS1* and HDAC proteins,
243 particularly HDAC11, are associated with tau tangles in excitatory neurons and plaque burden in
244 microglia (Fig. 6D-I). These findings indicate that *OIP5-AS1* may contribute to AD pathology through
245 epigenetic regulation in a cell-type-specific and context-dependent manner. Notably, the interaction
246 between *OIP5-AS1* and HDAC11 in excitatory neurons was strongly associated with tau tangle burden
247 in the hippocampus and medial temporal lobe (Fig. 6D, 6E). Given that tau pathology typically originates
248 in these regions and progresses to other cortical areas, our findings suggest that the interaction
249 between *OIP5-AS1* and HDAC11 may play a central role in tau progression and early hippocampal
250 vulnerability.

251 **Limitations**

252 This study has several inherent limitations. First, our spatial transcriptomics (ST) samples were
253 collected exclusively from non-Latino white females, limiting the generalizability of our findings to
254 younger individuals, males, or other racial and ancestral groups. Second, the 10x Visium platform relies
255 on polyadenylated (poly(A)) RNA capture, which excludes non-polyadenylated lncRNAs as well as

256 those with alternative 3' end processing or shorter poly(A) tails. Third, the platform's resolution of 55
257 μm constrains our ability to resolve cell-type-specific lncRNA expression within the spatial context.
258 Fourth, the relatively small sample size of the study reduces statistical power, likely leading to an
259 underestimation of the total number of AD-associated DE lncRNAs. Finally, while we provide insights
260 into potential functional roles of lncRNAs, including *OIP5-AS1*, experimental validation is necessary to
261 confirm their mechanistic contributions to AD pathogenesis.

262 **Conclusion and Future Directions**

263 This study provides ST profiles of lncRNAs in DLPFC of aged human brains. We mapped subregion-
264 specific lncRNA changes and identified hundreds of AD-associated DE lncRNAs, encompassing
265 previously known AD-associated lncRNAs, emerging immune-related lncRNAs, and novel lncRNAs.
266 These findings lay the groundwork for future investigations using higher-resolution spatial profiling
267 platforms, advanced lncRNA enrichment techniques, and co-detection of proteins in the same tissue
268 sections, enabling a more precise delineation of cell-type-specific lncRNA changes in response to
269 distinct AD pathologies. Additionally, we explored the potential interaction between *OIP5-AS1* and
270 HDACs in mediating AD-associated phenotypes. Emerging RNA-targeting technologies, such as
271 antisense oligonucleotides (ASOs)[63] and CRISPR-Cas13d[64,65], present exciting opportunities for
272 functional studies on *OIP5-AS1* and other AD-associated lncRNAs. Notably, a key limitation of HDAC
273 inhibitors in clinical trials has been their lack of specificity. *OIP5-AS1* may offer a promising avenue for
274 selectively modulating HDAC activity and stratifying patients for precision medicine.

275 **Acknowledgments**

276 We are grateful to those who agreed to donate their brains for research. We thank all the employees
277 at RADC for their support and assistance. This study was supported by NIA grants R01AG074082
278 and R01AG079223 (to Y.W.), P30AG10161, P30AG72975, R01AG015819, R01AG017917, and
279 U01AG61356 (to D. A. B.), and R01AG061798 (to C.G.).

280 **Author contributions**

281 B.N., D.R.A., K.P.L., S.T., R.A.V., T.C., and A.I. performed data analysis. D.R.A. and S.D.T.
282 conducted ST experiments. J.X. performed ST data processing. M.F., V.M., and P.L.D. provided
283 snRNA-seq data. H.V. and N.A.K. conducted RNAScope and IHC experiments. Y.W., B.N., D.R.A.,
284 and K.P.L. wrote the manuscript. D.A.B. runs the parent ROSMAP study and provides critical input.
285 Y.W. conceived and directed this study, overseeing research activities and leading manuscript
286 preparation. All authors reviewed and approved the final manuscript.

Lead Contact

Further information and requests may be directed to the corresponding author Yanling Wang (Yanling_Wang@rush.edu)

Materials Availability

This study did not generate new unique reagents.

Data Availability

Subregion- and cell-type-enriched lncRNAs, ST gene expression modules and AD-differential genes are provided in the Supplementary Information. Raw and normalized count matrices of the ST data is available at Synapse under accession code syn53141470.

Online Methods

Tissue collection for Spatial Transcriptomics

The human brain tissues were obtained through the ROSMAP (Religious Orders Study and Rush Memory and Aging Project) cohort studies at the Rush Alzheimer's Disease Center, Rush University Medical Center (RUMC), Chicago, IL[66]. Both studies were approved by the Institutional Review Board of RUMC. Written informed consent was obtained as was a repository consent and an Anatomic Gift Act, in compliance with national ethical guidelines. We selected 13 female individuals clinically diagnosed as AD and 8 controls with no cognitive impairment (NCI) based on criteria as previously reported[67–69]. The brain tissue of those individuals had RIN> 5 and minimal freezing artifacts. Frozen brain blocks of the right-hemisphere DLPFC were cut (~ 1 cm^3), transferred on dry ice, and stored at -80C.

Frozen brain blocks were embedded in OCT and cryosectioned coronally to a thickness of 10 µm using a Leica CM1950 cryostat set at -17C. Sectioning was done in sets of three (middle section for ST and two adjacent sections for IF), with 10-50 µm between each set. Sections were attached to Visium slides and stored at -80C in a slide mailer for up to one week before proceeding with spatial transcriptomics. ST-adjacent sections were attached to pre-labeled Leica superfrost plus slides and stored at -80C in slide mailers for up to two weeks before proceeding with immunohistochemistry.

Spatial Transcriptomics

Spatial Transcriptomics was performed according to the Visium Spatial Gene Expression User Guide (10X Genomics; CG000239). Briefly, cryosectioned tissue on Visium slides was transferred from -80C

316 to the lab on dry ice and quickly thawed for 1 min on a heat block at 37C, then immediately
317 transferred to methanol pre-equilibrated to -20C and fixed at -20C for 30 min. Sections were then
318 stained with hematoxylin and eosin, and brightfield images were acquired with a Nikon Ti2 with NIS-
319 Elements AR 5.11.01 64-bit software. After imaging, tissues were immediately permeabilized in 0.1%
320 pepsin diluted in 0.1 M HCl for 18 min at 37C. Reverse transcription, second-strand synthesis, cDNA
321 amplification (15 cycles), and library construction were performed according to the manufacturer's
322 instructions. For the first four individuals (#2, 8, 12, and 18), protocol version 'Rev A' was followed,
323 and the sample index PCR was 12 cycles. For the remaining samples, protocol version 'Rev D' was
324 followed, and the sample index PCR was 13-14 cycles. Library concentration was quantified by Qubit
325 1x dsDNA HS using a SpectraMax M3 plate reader. Library concentration and size distribution were
326 assessed by Fragment Analyzer (Agilent). Sequencing was performed in three batches on an Illumina
327 NovaSeq, targeting a minimum of 50,000 raw reads per spot.

328 **Spatial transcriptomics sequencing data processing**

329 Sequencing data were pre-processed with the Space Ranger pipeline (10x Genomics), which
330 mapped the barcodes against the human genome (Gencode 27), generated FASTQ files, and
331 generated a count matrix for each section. The individual files were then merged into a Seurat object
332 (Seurat v4.2.0) and were processed in R. We calculated per-spot quality metrics and spots with low-
333 measured genes (< 500) were removed. The Seurat::SCTransform function was used to normalize
334 and scale the UMI counts based on regularized negative binomial regression. Principal component
335 analysis (PCA) was performed on the top 3000 variable genes. Using the top 50 PCs and accounting
336 for technical and biological covariates such as age, RIN, library batch, and donor, we integrated the
337 datasets using the Harmony package (v0.1.0). We explored various tools for data integration and
338 chose Harmony for its high performance, usability, and scalability. We only used Harmony integration
339 to identify clusters corresponding to brain regions. All downstream analyses (differential gene
340 expression, cell proportion estimates, and ligand-receptor analysis) were performed on pre-
341 integration count data. After visualizing the standard deviation attributed to each Harmony embedding
342 as an elbow plot, we decided to use the top 10 Harmony embeddings. We applied Seurat::runUMAP
343 to compute UMAP (uniform manifold approximation and projection) dimension reduction and
344 Seurat::findNeighbors and Seurat::findClusters to identify clusters based on a shared nearest
345 neighbor (SNN) clustering algorithm (Louvain clustering with resolution set to 0.3; all other
346 parameters default). This resulted in 10 clusters, which were annotated based on their canonical
347 markers and spatialLIBD (v7.5) to the closest anatomical cortical layer (L1, L2-3, L3-5, L5, L6), white
348 matter (WM), meninges, and specific cellular subpopulations, namely cells with high expression of

349 hemoglobin genes ('Blood Vessel') and SST/NPY ('Interneuron'). The last identified cluster, which
350 carried a glial signature, had very few spots and so was not included in downstream analyses.
351 Seurat::FindMarkers was used to identify cluster-enriched (e.g. subregion-specific) lncRNAs reported
352 in Fig. 2A and Table S1. For Fig. 2A, a log2FC cutoff of 0.1 was employed resulting in 50 lncRNAs.

353 **Co-expression network analysis in spatial transcriptomics**

354 The modules of co-expressed genes were derived using the Speakeasy (SE) algorithm v1, Matlab
355 version[16]. We created pseudo-bulk gene expression by summing the counts per donor, then splitting
356 by UMAP cluster. Lowly expressed genes (less than 1 count per million, CPM) were removed, and
357 the variancePartition R function was applied to capture the major sources of variation, as previously
358 described[14]. The input for SE consisted of the residuals after normalization using tmm.voom and
359 adjustment for library batch, RIN, age, and PMI. We built the modules separately for each UMAP
360 cluster, using the results from 100 initializations of SE and Spearman correlation. This resulted in 193
361 modules, each with at least 30 genes (L1 = 30, L2-3 = 21, L3-5 = 20, L5 = 20, L6 = 20, Meninges =
362 33, WM = 20, and Blood Vessels = 29). The module assignments are provided in Table S2.

363 ***Functional Enrichment Analysis (FEA)***
364 Each module was annotated using the gprofiler software (v2_0.2.1) via the g:GOSt R function [70]. This
365 tool maps genes to functional information sources and detects statistically significantly enriched
366 terms. These sources include the GO database, pathways from KEGG, Reactome, and
367 WikiPathways, miRNA targets from miRTarBase, regulatory motif matches from TRANSFAC, tissue
368 specificity from the Human Protein Atlas, protein complexes from CORUM, and human disease
369 phenotypes from the Human Phenotype Ontology. For multiple testing correction, we used the default
370 g:SCS method unless otherwise specified. The FEA results are available in Table S4.

371 ***Module Preservation (MP) Analysis***
372 To assess whether the modules were preserved across distinct UMAP clusters, we used the MP
373 function from the WGCNA R package (v1.70-3)[71]. Pairwise comparisons were performed for all 193
374 modules. We then estimated the mean and variance of the preservation statistic under the null
375 hypothesis that there is no relationship between module assignments in the reference and test
376 datasets. Fifteen distinct preservation statistics were calculated (e.g., module density, mean
377 expression, connectivity), each standardized by its mean and variance to define a Z statistic for each
378 preservation measure. Under these assumptions, each Z statistic follows a normal distribution if the
379 module is not preserved. To compare preservation across modules, we calculated a composite
380 preservation measure using the following equation:

381

382 $$Zsummary = \frac{Zdensity + Zconnectivity}{2}$$

383

384 Modules with Z < 2 were considered not preserved, those with Z between 2 and 10 were considered
385 preserved, and modules with Z > 10 were considered highly preserved. Zsummary stats are available
386 in Table S3.

387 **Statistical analysis to identify AD-differential genes**

388 For each brain section of a subject, we summed the UMI counts of all spots belonging to a subregion
389 to generate a pseudobulk estimate for each gene. We only kept expressed genes with counts per
390 million (CPM) > 1 in at least 80% of the brain sections, resulting in 1,578 lncRNAs and 13,808
391 mRNAs. With the pseudobulk estimates, we estimated the library sizes of the brain sections using the
392 trimmed mean of M-values (TMM) of edgeR[72] (edgeR_3.36.0) and transformed the pseudobulk
393 estimates into $\log_2$ CPM using voom-limma (limma_3.50.1). For each subregion, we excluded brain
394 sections with <50 spots. To contrast the normalized pseudobulk expression between AD and controls,
395 we applied linear mixed models (LMM), accounting for age, PMI, RIN, and batch as fixed effects and
396 modeled within-subject correlation with a random effect. We declared significance at an α of 0.05 with
397 false discovery rate (FDR) correction across all genes and all subregions.

398 For interpretation, we applied GSEA[73] with AD-differential t-values of each subregion as scores, and
399 GO terms and canonical pathways as genesets. To characterize lncRNAs with respect to brain cell
400 types, we used the pseudobulk expression data from a published snRNAseq dataset of 424
401 ROSMAP individuals[15]. For each of the major cell types, we contrasted pseudobulk expression of AD
402 subjects vs. controls using multiple regression, accounting for age, PMI, RIN, and batch. For further
403 comparison, we repeated this AD-differential expression analysis with bulk DLPFC RNA-seq data
404 from 1049 individuals[20].

405 **Follow-up Analysis on *OIP5-AS1***

406 We used the eQTL statistics from the published snRNAseq dataset[15]. We first assembled the eQTL
407 statistics from all SNPs within 1Mb from the transcription start site of *OIP5-AS1*. This was done for six
408 major brain cell types (astrocytes, excitatory neurons, inhibitory neurons, microglia, oligodendrocytes,
409 and OPC) that showed adequate expression across subjects. We then applied mvSuSiE[36], which
410 aggregates the statistics across SNPs and cell types to estimate the posterior inclusion probability
411 that a given SNP casually affects expression of *OIP5-AS1*.

412 In addition, we further tested the interaction effects of *OIP5-AS1* and HDACs on 3 categories of AD
413 traits: cognitive decline, neuritic plaques, and tau tangles. For cognitive decline, scores from tests on
414 episodic memory (ep), semantic memory (se), working memory (wo), presentation speed (ps), and
415 presentation order (po) were examined with their aggregate (global) being the trait of focus. For
416 neuritic plaques, measurements were taken from medial frontal (mf), medial temporal (mt), anterior
417 gyrus (ag), entorhinal cortex(ec), and hippocampus (hip) with their aggregate as the trait of focus. For
418 tau tangles, measurements were taken from mf, ag, ec, hip, inferior temporal (it), cingulate gyrus (cg),
419 and mesial temporal (mes_t) with their aggregate as the trait of focus. For each of the six major brain
420 cell types[15] and each HDAC protein detected in a bulk DLPFC dataset (HDACs 2, 4, 5, 6, 8, 11)[37], we
421 applied multiple regression to model an AD trait by the main effect of *OIP5-AS1* expression, the main
422 effect of a HDAC protein, and their interaction effect, while accounting for age, PMI, RIN, and batch.
423 To aid interpretation, we further divided the subjects into tertiles based on *OIP5-AS1* expression and
424 examined how each AD trait relates to HDAC abundance for each tertile. The same analysis was
425 repeated with HDAC protein abundance replaced by HDAC expression level from the snRNA-seq
426 dataset.

427 **RNAscope and Immunofluorescence co-staining and analysis**

428 Human FFPE DLPFC sections were stained with neuron (MAP2; Sigma #M2320-100UL) and
429 microglia (IBA1; Wako #019-19741) markers followed by RNAscope with Hs-OIP5-AS1-O1-C1 probe
430 (ACD #1559738-C1) using a Bond-Rx research stainer (Leica Biosystems) using an Opal 6-plex
431 detection kit (Akoya Biosciences #NEL871001KT). Briefly, sections were baked for 30 min at 60 °C
432 prior to dewaxing for 30 s at 72 °C. Sections were antigen retrieved using HIER with a pH 6.0 citrate
433 buffer solution (Leica Biosystems #AR9961) for 20 min at 100 °C followed by 10 min peroxide block.
434 MAP2 (1:100) was incubated for 30 min followed by 10 min Opal polymer HRP Ms+Rb and 10 min
435 Opal signal development with Opal 520 diluted at 1:100. Sections were antigen retrieved for 20 min in
436 ph 6.0 buffer again and the process is repeated with IBA1 (1:500) paired with Opal 690 (1:150). The
437 sections were then stained with RNAscope probe against *OIP5-AS1* using RNAScope LS Multiplex
438 Fluorescent Reagent Kit (ACD #322800) according to the manufacturer with the following
439 modifications. The sections were antigen retrieved using HIER with a pH 6.0 buffer for 20 min at 100
440 °C, washed, and treated with ACD Protease III for 15 min at 40 °C prior to probe hybridization for 2 h
441 at 40 °C. Opal 620 (1:500) was used for signal development. Slides were counter stained with 10X
442 spectral DAPI for 5 min before mounting. Imaging was performed using Phenocycler-Fusion 2.0
443 (Akoya Biosciences) at 40X. Images were spectrally umixed using inForm (Akoya Biosciences) and
444 composite TIFs exported to QuPath (v0.3.2) for quantitative analysis. Regions of interest that

445 encompassed cortical layers were identified and selected as ROIs based on tissue cytoarchitecture
446 patterns from nuclei and neuron stains. Cells were defined in each ROI using QuPath Cell Detection
447 tool with the following parameters, requested pixel size = 0.5μm, background radius = 8μm, median
448 filter radius =0μm, Sigma value for Gaussian filter = 1.5μm, minimum nucleus area = 10μm2 ,
449 maximum nucleus area =400μm2 , and intensity threshold = 10. Cell parameters include a cell
450 expansion of 5 μm from the cell nucleus and general parameters include smoothing of the detected
451 nucleus/cell boundaries. To quantify OIP5-AS1, subcellular spot parameters were set to detection
452 threshold = 0.08, split by intensity and shape to true, expected spot size = 0.05μm2, min spot size =
453 0.01μm2, max spot size =1μm2 and include clusters set to true. For cell type specific expression,
454 cells were thresholded on their MAP2 and IBA1 mean cell intensity by section and cells of ambiguous
455 identity were not included in the analysis.

456

457

458

459

460

461

462

463

464

465

466

467

468

469

470

References

1. Mattick, J. S. *et al.* Long non-coding RNAs: definitions, functions, challenges and recommendations. *Nat. Rev. Mol. Cell Biol.* **24**, 430–447 (2023).
2. Statello, L., Guo, C.-J., Chen, L.-L. & Huarte, M. Gene regulation by long non-coding RNAs and its biological functions. *Nat. Rev. Mol. Cell Biol.* **22**, 96–118 (2020).
3. Wang, K. C. & Chang, H. Y. Molecular mechanisms of long noncoding RNAs. *Mol. Cell* **43**, 904–914 (2011).
4. Guttman, M. *et al.* Chromatin signature reveals over a thousand highly conserved large non-coding RNAs in mammals. *Nature* **458**, 223–227 (2009).
5. Kung, J. T. Y., Colognori, D. & Lee, J. T. Long noncoding RNAs: past, present, and future. *Genetics* **193**, 651–669 (2013).
6. Djebali, S. *et al.* Landscape of transcription in human cells. *Nature* **489**, 101–108 (2012).
7. Cabili, M. N. *et al.* Integrative annotation of human large intergenic noncoding RNAs reveals global properties and specific subclasses. *Genes Dev.* **25**, 1915–1927 (2011).
8. Derrien, T. *et al.* The GENCODE v7 catalog of human long noncoding RNAs: analysis of their gene structure, evolution, and expression. *Genome Res.* **22**, 1775–1789 (2012).
9. Wu, X., Xia, P., Yang, L., Lu, C. & Lu, Z. The roles of long non-coding RNAs in Alzheimer's disease diagnosis, treatment, and their involvement in Alzheimer's disease immune responses. *Noncoding RNA Res.* **9**, 659–666 (2024).
10. Policarpo, R. & d'Ydewalle, C. Missing lnc(RNAs) in Alzheimer's Disease? *Genes* **13**, (2021).
11. Lan, Z., Chen, Y., Jin, J., Xu, Y. & Zhu, X. Long non-coding RNA: Insight into mechanisms of Alzheimer's disease. *Front. Mol. Neurosci.* **14**, 821002 (2021).
12. Huang, Z., Zhao, J., Wang, W., Zhou, J. & Zhang, J. Depletion of LncRNA NEAT1 rescues mitochondrial dysfunction through NEDD4L-dependent PINK1 degradation in animal models of Alzheimer's disease. *Front. Cell. Neurosci.* **14**, 28 (2020).
13. Riva, P., Ratti, A. & Venturin, M. The Long Non-Coding RNAs in Neurodegenerative Diseases: Novel Mechanisms of Pathogenesis. *Curr. Alzheimer Res.* **13**, 1219–1231 (2016).
14. Avey, D. R. *et al.* Uncovering plaque-Glia niches in human Alzheimer's Disease brains using spatial transcriptomics. *bioRxivorg* (2024) doi:10.1101/2024.09.05.611566.
15. Fujita, M. *et al.* Cell subtype-specific effects of genetic variation in the Alzheimer's disease brain. *Nat. Genet.* **56**, 605–614 (2024).
16. Gaiteri, C. *et al.* Identifying robust communities and multi-community nodes by combining top-down and bottom-up approaches to clustering. *Sci. Rep.* **5**, 1–14 (2015).
17. Li, D. *et al.* Insights into lncRNAs in Alzheimer's disease mechanisms. *RNA Biol.* **18**, 1037–1047 (2021).
18. Bellenguez, C. *et al.* New insights into the genetic etiology of Alzheimer's disease and related dementias. *Nat. Genet.* **54**, 412–436 (2022).
19. Law, C. W., Chen, Y., Shi, W. & Smyth, G. K. voom: Precision weights unlock linear model analysis tools for RNA-seq read counts. *Genome Biol.* **15**, R29 (2014).
20. Mostafavi, S. *et al.* A molecular network of the aging human brain provides insights into the pathology and cognitive decline of Alzheimer's disease. *Nat. Neurosci.* **21**, 811–819 (2018).
21. Shukla, S. & Tekwani, B. L. Histone deacetylases inhibitors in neurodegenerative diseases, neuroprotection and neuronal differentiation. *Front. Pharmacol.* **11**, 537 (2020).
22. Govindarajan, N. *et al.* Reducing HDAC6 ameliorates cognitive deficits in a mouse model for

515 Alzheimer's disease. *EMBO Mol. Med.* **5**, 52–63 (2013).
516 23. Onishi, T. *et al.* A novel orally active HDAC6 inhibitor T-518 shows a therapeutic potential for
517 Alzheimer's disease and tauopathy in mice. *Sci. Rep.* **11**, 15423 (2021).
518 24. Yang, S.-S., Zhang, R., Wang, G. & Zhang, Y.-F. The development prospection of HDAC
519 inhibitors as a potential therapeutic direction in Alzheimer's disease. *Transl. Neurodegener.* **6**, 19
520 (2017).
521 25. Zhang, M. *et al.* Histone deacetylase inhibitors VPA and WT161 ameliorate the pathological
522 features and cognitive impairments of the APP/PS1 Alzheimer's disease mouse model by
523 regulating the expression of APP secretases. *Alzheimers. Res. Ther.* **16**, 15 (2024).
524 26. Kumar, V., Kundu, S., Singh, A. & Singh, S. Understanding the role of histone deacetylase and
525 their inhibitors in neurodegenerative disorders: Current targets and future perspective. *Curr.*
526 *Neuropharmacol.* **20**, 158–178 (2022).
527 27. Ru, J. *et al.* Technologies of targeting histone deacetylase in drug discovery: Current progress
528 and emerging prospects. *Eur. J. Med. Chem.* **261**, 115800 (2023).
529 28. Yang, J.-H. *et al.* LncRNA OIP5-AS1-directed miR-7 degradation promotes MYMX production
530 during human myogenesis. *Nucleic Acids Res.* **50**, 7115–7133 (2022).
531 29. Zhuang, A. *et al.* Loss of the long non-coding RNA OIP5-AS1 exacerbates heart failure in a sex-
532 specific manner. *iScience* **24**, 102537 (2021).
533 30. Hunkler, H. J. *et al.* The long non-coding RNA Cyrano is dispensable for pluripotency of Murine
534 and human pluripotent stem cells. *Stem Cell Reports* **15**, 13–21 (2020).
535 31. Kotake, Y., Matsunaga, N., Wakasaki, T. & Okada, R. OIP5-AS1 promotes proliferation of non-
536 small-cell lung cancer and head and neck squamous cell carcinoma cells. *Cancer Genomics*
537 *Proteomics* **18**, 543–548 (2021).
538 32. Wu, L., Liu, Y., Guo, C. & Shao, Y. LncRNA OIP5-AS1 promotes the malignancy of pancreatic
539 ductal adenocarcinoma via regulating miR-429/FOXD1/ERK pathway. *Cancer Cell Int.* **20**, 296
540 (2020).
541 33. Arunkumar, G. *et al.* LncRNA OIP5-AS1 is overexpressed in undifferentiated oral tumors and
542 integrated analysis identifies as a downstream effector of stemness-associated transcription
543 factors. *Sci. Rep.* **8**, 7018 (2018).
544 34. Gong, M. *et al.* OIP5 is a novel prognostic biomarker in clear cell renal cell cancer correlating
545 with immune infiltrates. *Front. Immunol.* **13**, 805552 (2022).
546 35. Li, Z. *et al.* Exosomal OIP5-AS1 attenuates cerebral ischemia-reperfusion injury by negatively
547 regulating TXNIP protein stability and inhibiting neuronal pyroptosis. *Int. Immunopharmacol.* **127**,
548 111310 (2024).
549 36. Zou, Y., Carbonetto, P., Xie, D., Wang, G. & Stephens, M. Fast and flexible joint fine-mapping of
550 multiple traits via the Sum of Single Effects model. *bioRxivorg* (2024)
551 doi:10.1101/2023.04.14.536893.
552 37. Johnson, E. C. B. *et al.* Large-scale deep multi-layer analysis of Alzheimer's disease brain
553 reveals strong proteomic disease-related changes not observed at the RNA level. *Nat. Neurosci.*
554 **25**, 213–225 (2022).
555 38. Jiang, C. *et al.* Identifying and functionally characterizing tissue-specific and ubiquitously
556 expressed human lncRNAs. *Oncotarget* **7**, 7120–7133 (2016).
557 39. de Goede, O. M. *et al.* Population-scale tissue transcriptomics maps long non-coding RNAs to
558 complex disease. *Cell* **184**, 2633–2648.e19 (2021).
559 40. Li, F. *et al.* The effect of BACE1-AS on β-amyloid generation by regulating BACE1 mRNA

560 expression. *BMC Mol. Biol.* **20**, 23 (2019).
561 41. Faghihi, M. A. *et al.* Expression of a noncoding RNA is elevated in Alzheimer's disease and
562 drives rapid feed-forward regulation of beta-secretase. *Nat. Med.* **14**, 723–730 (2008).
563 42. Zhang, W., Zhao, H., Wu, Q., Xu, W. & Xia, M. Knockdown of BACE1-AS by siRNA improves
564 memory and learning behaviors in Alzheimer's disease animal model. *Exp. Ther. Med.* **16**, 2080–
565 2086 (2018).
566 43. Modarresi, F. *et al.* Inhibition of natural antisense transcripts in vivo results in gene-specific
567 transcriptional upregulation. *Nat. Biotechnol.* **30**, 453–459 (2012).
568 44. Jiao, S.-S. *et al.* Brain-derived neurotrophic factor protects against tau-related neurodegeneration
569 of Alzheimer's disease. *Transl. Psychiatry* **6**, e907 (2016).
570 45. Ding, Y., Luan, W., Shen, X., Wang, Z. & Cao, Y. LncRNA BDNF-AS as ceRNA regulates the
571 miR-9-5p/BACE1 pathway affecting neurotoxicity in Alzheimer's disease. *Arch. Gerontol. Geriatr.*
572 **99**, 104614 (2022).
573 46. Ma, P. *et al.* Long non-coding RNA MALAT1 inhibits neuron apoptosis and neuroinflammation
574 while stimulates neurite outgrowth and its correlation with MiR-125b mediates PTGS2, CDK5 and
575 FOXQ1 in Alzheimer's disease. *Curr. Alzheimer Res.* **16**, 596–612 (2019).
576 47. Bernard, D. *et al.* A long nuclear-retained non-coding RNA regulates synaptogenesis by
577 modulating gene expression. *EMBO J.* **29**, 3082–3093 (2010).
578 48. Dong, L.-X. *et al.* LncRNA NEAT1 promotes Alzheimer's disease by down regulating micro-27a-
579 3p. *Am. J. Transl. Res.* **13**, 8885–8896 (2021).
580 49. Ke, S. *et al.* Long noncoding RNA NEAT1 aggravates Aβ-induced neuronal damage by targeting
581 miR-107 in Alzheimer's disease. *Yonsei Med. J.* **60**, 640–650 (2019).
582 50. Bútová, R. *et al.* LncRNAs LY86-AS1 and VIM-AS1 distinguish plasma cell leukemia patients
583 from multiple myeloma patients. *Biomedicines* **9**, 1637 (2021).
584 51. Kurniansyah, N. *et al.* An integrated multi-omics analysis of sleep-disordered breathing traits
585 implicates P2XR4 purinergic signaling. *Commun. Biol.* **6**, 125 (2023).
586 52. Tan, Y. *et al.* lncRNA-associated ceRNA network revealing the potential regulatory roles of
587 ferroptosis and immune infiltration in Alzheimer's disease. *Front. Aging Neurosci.* **15**, 1105690
588 (2023).
589 53. Bajic, V. P. *et al.* The X files: 'the mystery of X chromosome instability in Alzheimer's disease'.
590 *Front. Genet.* **10**, 1368 (2019).
591 54. Garcia, A. X., Xu, J., Cheng, F., Ruppin, E. & Schäffer, A. A. Altered gene expression in
592 excitatory neurons is associated with Alzheimer's disease and its higher incidence in women.
593 *Alzheimers Dement. (N. Y.)* **9**, e12373 (2023).
594 55. Sun, X. *et al.* The MAOA gene influences the neural response to psychosocial stress in the
595 human brain. *Front. Behav. Neurosci.* **14**, 65 (2020).
596 56. Ziermans, T. *et al.* Working memory brain activity and capacity link MAOA polymorphism to
597 aggressive behavior during development. *Transl. Psychiatry* **2**, e85 (2012).
598 57. Chua, G. N. L. *et al.* Differential dynamics specify MeCP2 function at nucleosomes and
599 methylated DNA. *Nat. Struct. Mol. Biol.* 1–9 (2024).
600 58. Chu, S.-L. *et al.* Phosphoglycerate kinase 1 acts as a cargo adaptor to promote EGFR transport
601 to the lysosome. *Nat. Commun.* **15**, 1021 (2024).
602 59. Vinokurov, A. Y. *et al.* HPRT1 deficiency induces alteration of mitochondrial energy metabolism
603 in the brain. *Mol. Neurobiol.* **60**, 3147–3157 (2023).
604 60. Wooten, S. & Smith, K. N. Long non-coding RNA OIP5-AS1 (Cyrano): A context-specific

605 regulator of normal and disease processes. *Clin. Transl. Med.* **12**, e706 (2022).
606 61. Mei, J. *et al.* OIP5-AS1 modulates epigenetic regulator HDAC7 to enhance non-small cell lung
607 cancer metastasis via miR-140-5p. *Oncol. Lett.* **20**, 7 (2020).
608 62. Kleaveland, B., Shi, C. Y., Stefano, J. & Bartel, D. P. A network of noncoding regulatory RNAs
609 acts in the mammalian brain. *Cell* **174**, 350–362.e17 (2018).
610 63. Mummery, C. J. *et al.* Tau-targeting antisense oligonucleotide MAPTRx in mild Alzheimer's
611 disease: a phase 1b, randomized, placebo-controlled trial. *Nat. Med.* **29**, 1437–1447 (2023).
612 64. Kuo, H.-C., Prupes, J., Chou, C.-W. & Finkelstein, I. J. Massively parallel profiling of RNA-
613 targeting CRISPR-Cas13d. *Nat Commun* **15**, (2024).
614 65. Wessels, H.-H. *et al.* Massively parallel Cas13 screens reveal principles for guide RNA design.
615 *Nat. Biotechnol.* **38**, 722–727 (2020).
616 66. Bennett, D. A. *et al.* Religious Orders Study and Rush Memory and Aging Project. *J. Alzheimers.*
617 *Dis.* **64**, S161–S189 (2018).
618 67. Bennett, D. A. *et al.* Natural history of mild cognitive impairment in older persons. *Neurology* **59**,
619 198–205 (2002).
620 68. Bennett, D. A. *et al.* Neuropathology of older persons without cognitive impairment from two
621 community-based studies. *Neurology* **66**, 1837–1844 (2006).
622 69. Bennett, D. A. *et al.* Decision rules guiding the clinical diagnosis of Alzheimer's disease in two
623 community-based cohort studies compared to standard practice in a clinic-based cohort study.
624 *Neuroepidemiology* **27**, 169–176 (2006).
625 70. Kolberg, L. *et al.* g:Profiler-interoperable web service for functional enrichment analysis and gene
626 identifier mapping (2023 update). *Nucleic Acids Res.* **51**, W207–W212 (2023).
627 71. Langfelder, P., Luo, R., Oldham, M. C. & Horvath, S. Is my network module preserved and
628 reproducible? *PLoS Comput. Biol.* **7**, e1001057 (2011).
629 72. Robinson, M. D., McCarthy, D. J. & Smyth, G. K. edgeR: a Bioconductor package for differential
630 expression analysis of digital gene expression data. *Bioinformatics* **26**, 139–140 (2010).
631 73. Subramanian, A. *et al.* Gene set enrichment analysis: A knowledge-based approach for
632 interpreting genome-wide expression profiles. *Proceedings of the National Academy of Sciences*
633 **102**, 15545–15550 (2005).

634

635

636

637

638

639

640

641

642

Main Figures

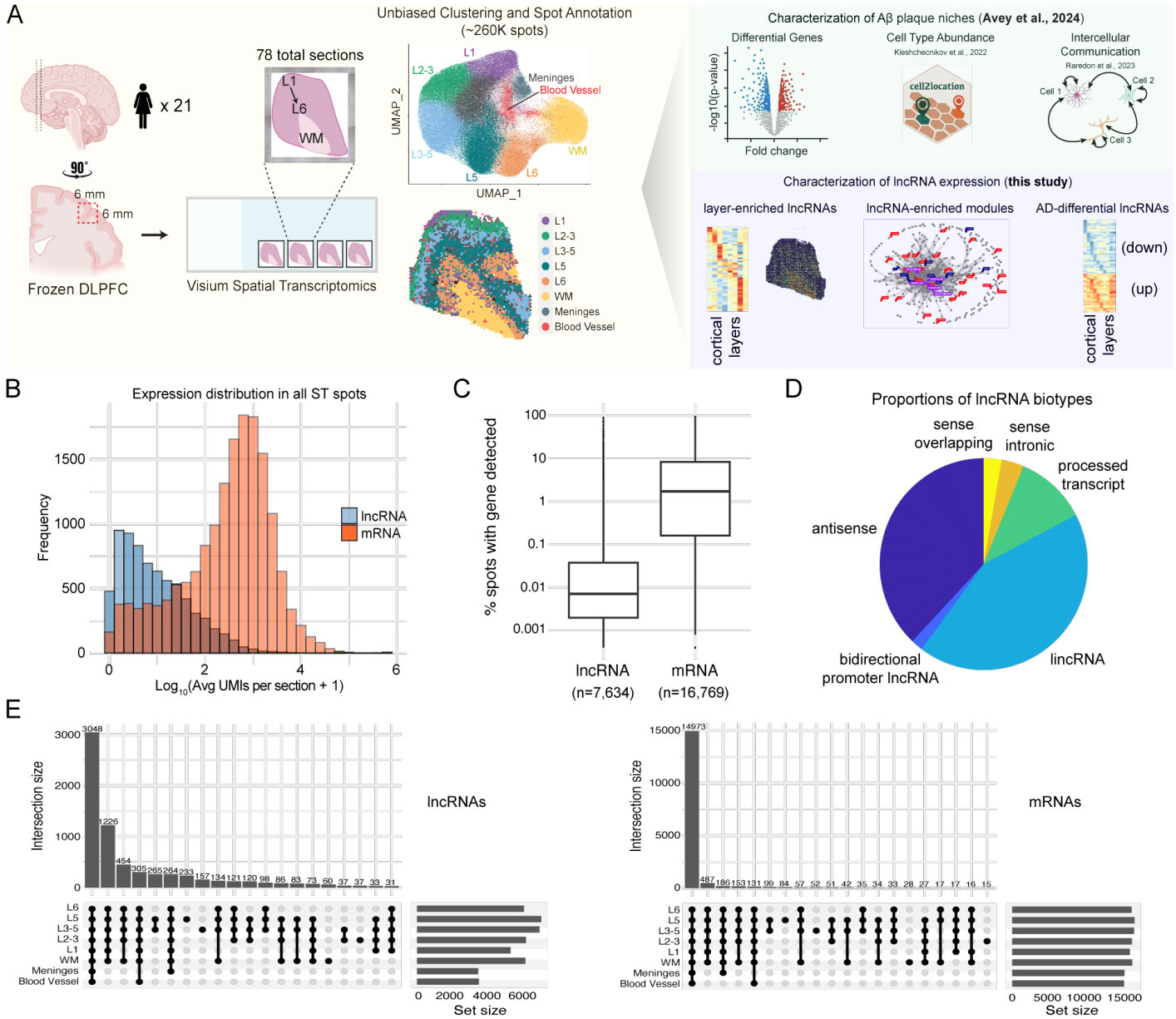

Figure 1. Spatial expression of lncRNAs. (A) Study overview. **(B)** Comparison of the expression distributions of lncRNAs and protein-coding genes (mRNAs). **(C)** Comparison of percentage of ST spots with non-zero expression for lncRNAs and mRNAs. **(D)** Proportion of detected lncRNAs (aggregated across subregions) belonging to each biotype. **(E)** Upset plots showing the numbers of lncRNAs (left) and mRNAs (right) detected in the top 20 most common intersections of subregions.

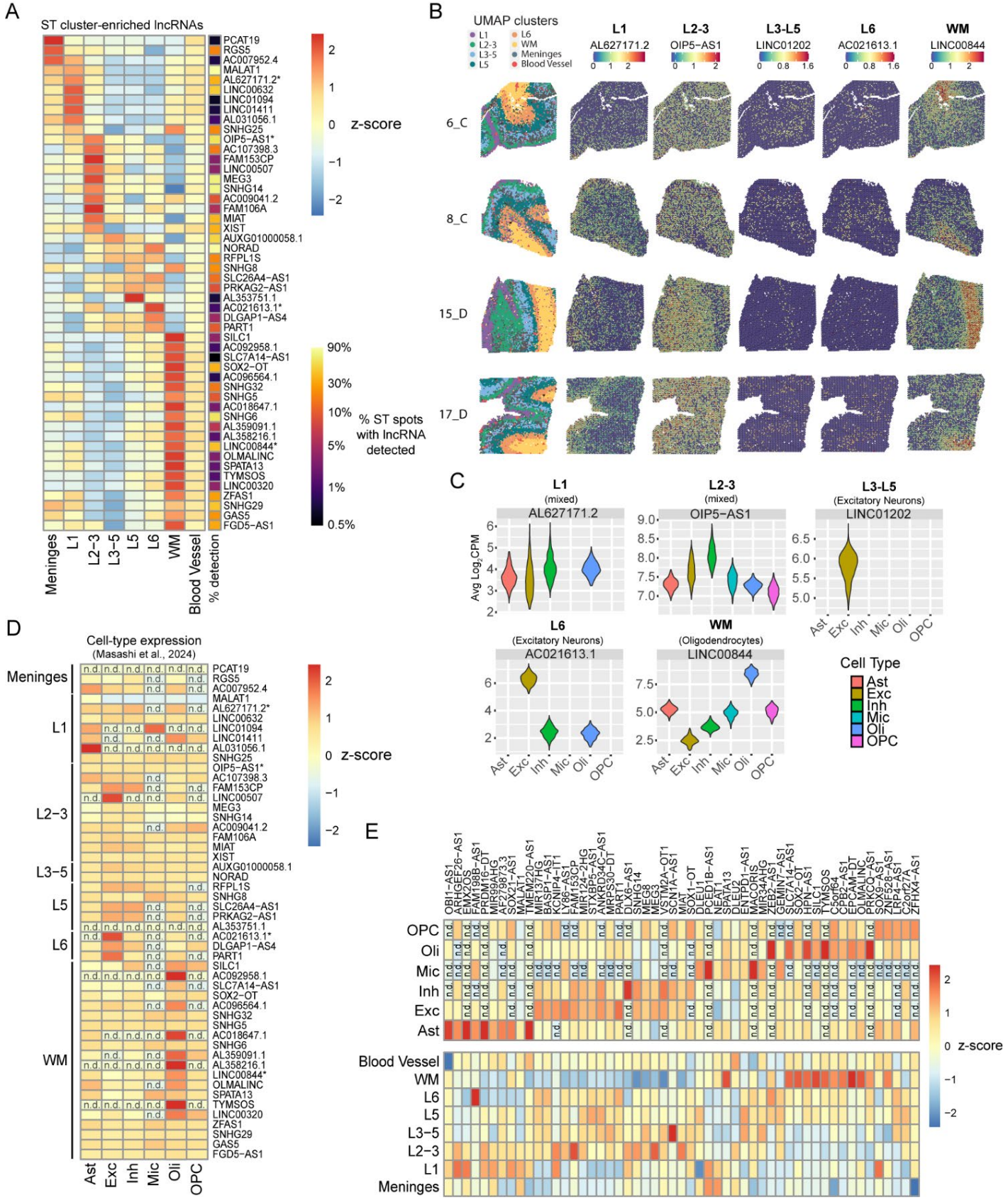

Figure 2. Subregion- and cell-type-enriched lncRNAs. (A) Heatmap showing scaled expression (z-score) of the top 50 subregion-specific lncRNAs. The last column to the right shows the percentage of spots with non-zero expression for each lncRNA (*exemplar lncRNAs shown in panel B). **(B)** UMAP and expression feature plots for 4 representative sections, showing 5 examples of lncRNAs with enriched expression in specific cortical layers or white matter (WM). **(C)** Violin plots showing expression distributions among 6 major brain cell types for the 5

lncRNAs shown in (B). **(D)** Scaled snRNA-seq expression of the same 50 subregion-specific lncRNAs shown in (A) for the 6 most abundant brain cell types (*exemplar lncRNAs shown in panel B; n.d.: not detected). **(E)** Scaled expression by cell type (top) and ST subregion (bottom) for the top 10 cell-type-specific lncRNAs from each of the 6 major brain cell types.

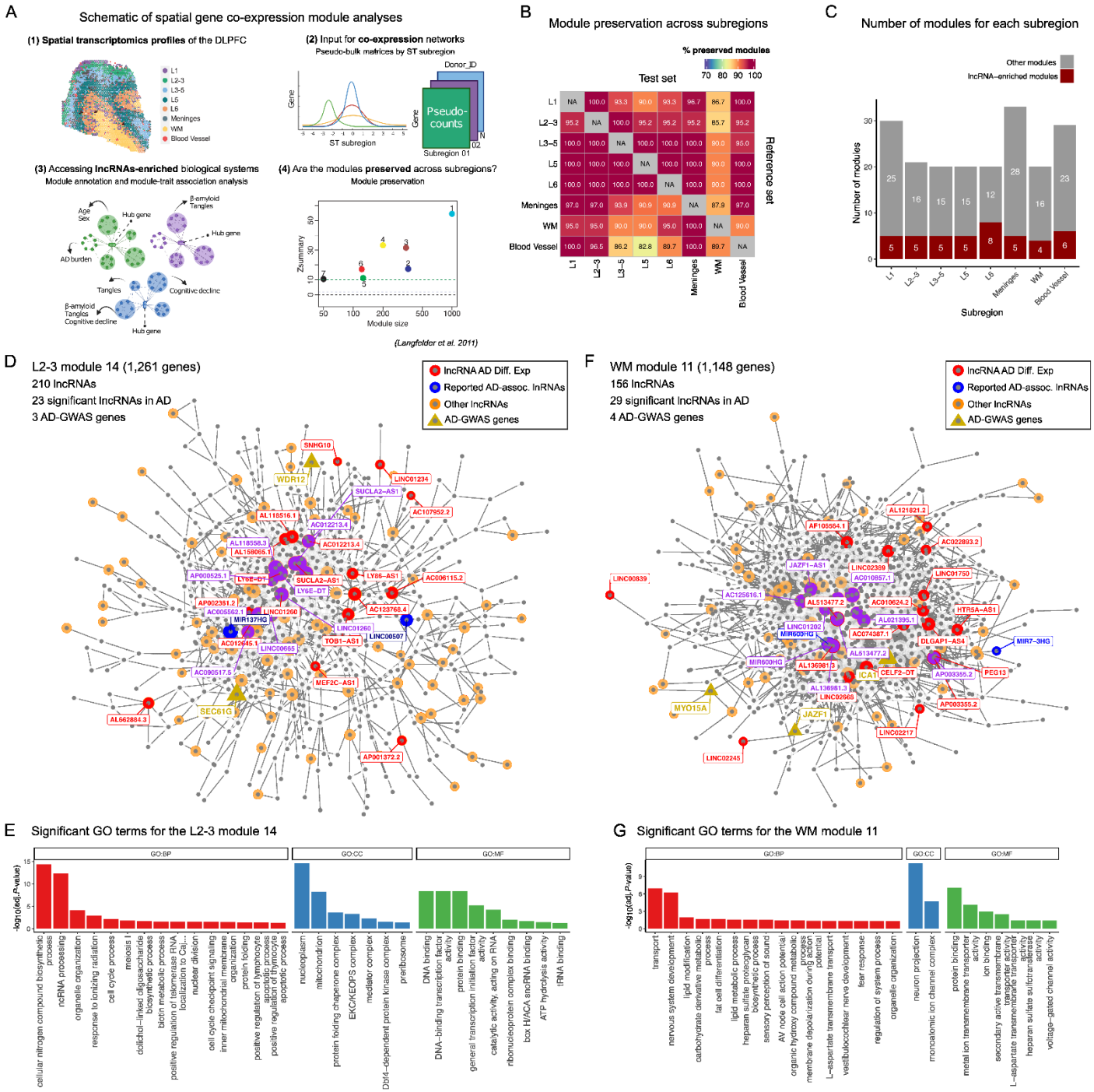

Figure 3. Subregion-specific gene modules.
(A) Schematic of gene expression module generation and downstream analyses. **(B)** Heatmap showing the percentage of preserved modules between each pair of subregions. **(C)** Stacked barplot shows the number of modules in each subregion. Red colors for the lncRNA-enriched modules. **(D)** Network connectivity map for L2-3 m14, illustrating high connectivity of lncRNAs (correlation > 0.9). **(E)** Enriched Gene Ontology (GO) terms (FDR at 0.05) from functional enrichment analysis of an example lncRNA-enriched module (L2-3 m14). **(F)** Network connectivity map for WM module 11, illustrating high connectivity of lncRNAs (correlation > 0.95). **(G)** Enriched GO terms (FDR at 0.05) from functional enrichment analysis for the WM module 11. **(E, G)** The GO biological process terms were collapsed, keeping only the top GO parent functions to avoid redundancy. The y-axis and bar size represent the significance in -$\log_{10}$(Adj. p-Value). GO biological process (BP), cellular component (CC), and GO molecular function (MF).

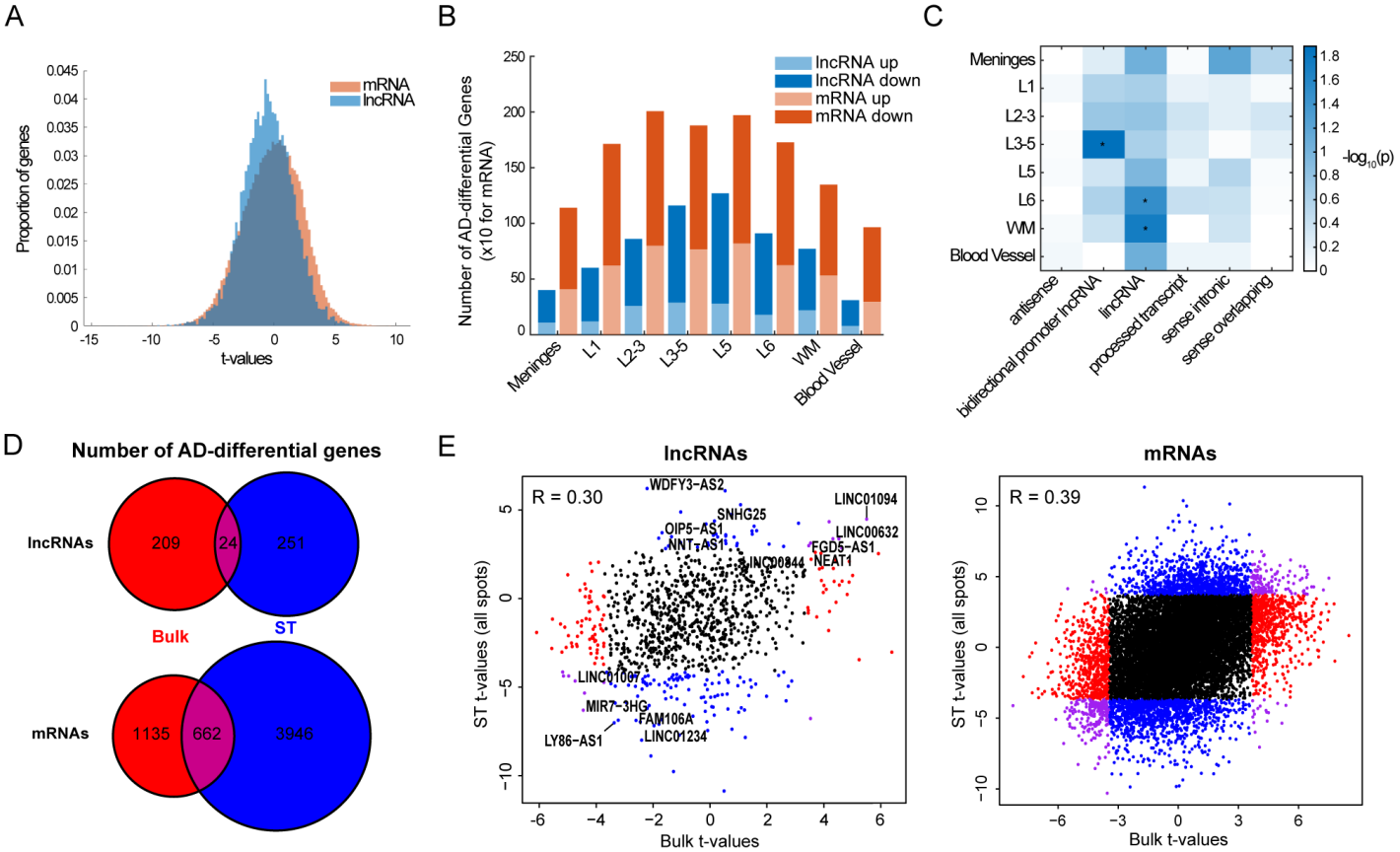

Figure 4. Differential lncRNAs and mRNAs in AD and cross-modality comparison with bulk RNA-seq. (A) Histogram showing the distribution of AD-differential t-values for mRNAs and lncRNAs. **(B)** Total numbers of AD-differential lncRNAs and mRNAs for each subregion. **(C)** Heatmap showing the enrichment of AD-differential lncRNAs for specific biotypes. **(D)** Overlaps in AD-differential lncRNAs and mRNAs between ST and bulk RNA-seq. **(E)** Scatterplots of ST (y-axis) vs. bulk RNA-seq (x-axis) AD-differential t-values for lncRNAs (left) and mRNAs (right). Correlation value (R) is shown at the top left of each plot.

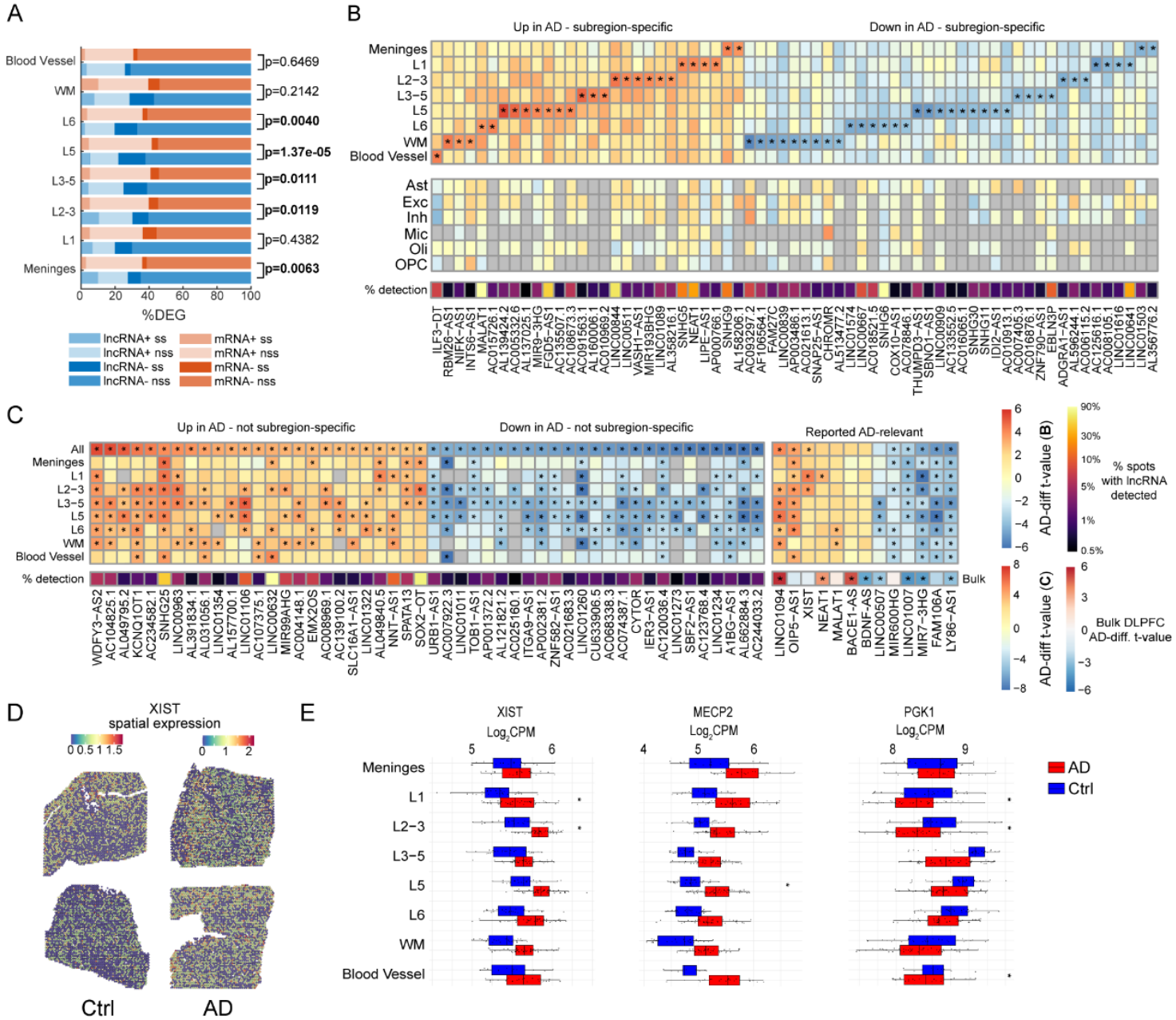
A
Blood Vessel
WM
L6
L5
L3-5
L2-3
L1
Meninges
p=0.6469
p=0.2142
p=0.0040
p=1.37e-05
p=0.0111
p=0.0119
p=0.4382
p=0.0063
%DEG
lncRNA+ ss
lncRNA+ nss
lncRNA- ss
lncRNA- nss
mRNA+ ss
mRNA+ nss
mRNA- ss
mRNA- nss
B
Up in AD - subregion-specific
Down in AD - subregion-specific
Meninges
L1
L2−3
L3−5
L5
L6
WM
Blood Vessel
Ast
Exc
Inh
Mic
Oli
OPC
% detection
C
Up in AD - not subregion-specific
Down in AD - not subregion-specific
Reported AD-relevant
AD-diff t-value (B)
% spots with lncRNA detected
AD-diff t-value (C)
Bulk DLPFC AD-diff. t-value
Bulk
D
XIST spatial expression
Ctrl
AD
E
XIST Log2CPM
MECP2 Log2CPM
PGK1 Log2CPM
AD
Ctrl
F
MALAT1
XIST
FGD5-AS1
NNT-AS1
OIP5-AS1
SNAP25-AS1
NEAT1
KCNQ1OT1
SPATA13
ARMCX5-GPRASP2
APOPTOTIC PROCESS
CELL JUNCTION ORGANIZATION
CELL MOTILITY
CHROMATIN ORGANIZATION
CHROMATIN REMODELING
EPIGENETIC REGULATION OF GENE EXPRESSION
HDAC3 TARGETS DN
HETEROCHROMATIN ORGANIZATION
NCRNA METABOLIC PROCESS
POSITIVE REGULATION OF RNA METABOLIC PROCESS
PROTEIN CONTAINING COMPLEX ORGANIZATION
REGULATION OF CELL DEATH
REGULATION OF CELL PROJECTION ORGANIZATION
REGULATION OF CELLULAR COMPONENT BIOGENESIS
REGULATION OF DEFENSE RESPONSE
REGULATION OF INTRACELLULAR SIGNAL TRANSDUCTION
RNA BINDING
SIGNALING RECEPTOR BINDING
SMALL GTPASE MEDIATED SIGNAL TRANSDUCTION
SYNAPSE ORGANIZATION
Signed -log10(p)
G
Meninges
L1
L2−3
L3−5
L5
L6
WM
Blood Vessel
HDAC3
HDAC10
HDAC7
HDAC1
HDAC11
HDAC4
HDAC2
HDAC9
HDAC8
HDAC4−AS1
HDAC5
HDAC6
ST AD-diff t-value

Figure 5. Characterization of AD-differential lncRNAs detected by ST. (A) The percentage of DEGs in each ST subregion, split by lncRNA/mRNA, up/down in AD, and whether they are subregion-specific (ss) or not (nss). Fisher's exact test was applied to assess differences in subregion-specificity between lncRNA and mRNA with p-values indicated. **(B)** (top) Heatmap showing t-values of AD-differential lncRNAs passing FDR correction specifically for one ST subregion, i.e. subregion-specific (*p<5e-4 in designated subregion and p>0.001 in all others). (bottom) AD-differential t-values for 6 brain cell types. An additional row below shows the percentage of ST spots with non-zero expression for each lncRNA. **(C)** (left) Heatmap showing t-values of AD-differential lncRNAs passing FDR correction in two or more ST subregions, i.e. not subregion-specific (*p<5e-4). An additional row below shows the percentage of ST spots with non-zero expression for each lncRNA. (right) AD-differential t-values for a subset of 13 lncRNAs with previously reported AD association, including t-values from DLPFC bulk RNA-seq below. **(D)** XIST spatial expression plots for two control (Ctrl) and two AD sections. **(E)** Boxplots of subregion-specific pseudobulk expression from ST data for XIST, MECP2, and PGK1 (X-linked genes), all of which show altered expression in AD in one or more subregions. **(F)** Sankey diagram and heatmap showing a subset of enriched genesets and AD differential lncRNAs belonging to those genesets. (**G**) A subset of HDAC genes display AD-differential expression in specific ST subregions (*p<5e-4).

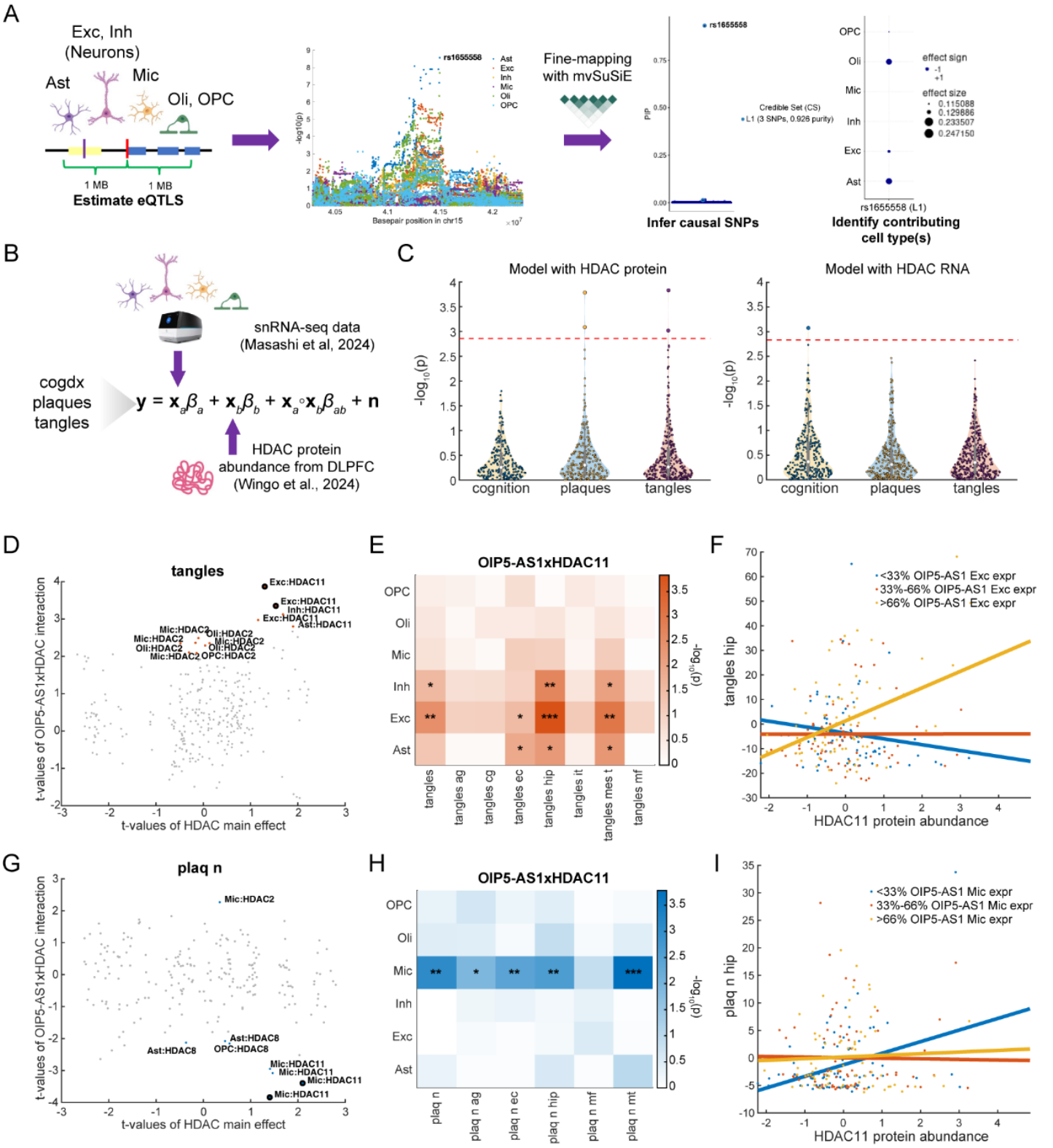

Figure 6. Genetic analysis of *OIP5-AS1* and its interaction with HDAC. (A) Colocalization analysis of *OIP5-AS1* eQTLs across major brain cell types. Applying multivariate colocalization found rs1655558 to be a potential driver of *OIP5-AS1* expression in astrocytes, oligodendrocytes, and excitatory neurons (Ast: Astrocyte, Exc: excitatory, Inh: Inhibitory, Mic: Microglia, Oli: Oligodendrocyte, OPC: Oligodendrocyte progenitor cell, PIP: posterior inclusion probability; cartoon cell type images created in BioRender.com). **(B)** Summary of *OIP5-AS1*xHDAC interaction analysis. snRNAseq[14] and proteomic[37] data from human DLPFC were used to associate the statistical interaction between *OIP5-AS1* expression level (in specific cell types) and protein abundance of each of six HDACs with AD phenotypes, including cognitive decline (cogdx), amyloid plaques, and tau tangles. Cognition was assessed over multiple domains and pathologies were measured in

820 multiple brain regions. **(C)** Each point in the violin plot represents the –log10(p) of the interaction effect of
821 *OIP5-AS1* and HDAC for a given combination of cell type, HDAC, and AD phenotype. Higher associations
822 were observed for plaques and tangles. **(D)** Scatterplots showing t-values of the HDAC main effect (x-axis) and
823 the *OIP5-AS1xHDAC* interaction for tangles measured in multiple brain regions**.** Dots are colored but not
824 circled if interaction $p<0.05$ and an order of magnitude lower than the main effect p-value. Circled dots are
825 interactions passing multiple comparison correction for the number of HDACs and cell types. *OIP5-*
826 *AS1*xHDAC11 interaction shows the strongest association with tangles. (**E**) Heatmap of *OIP5-AS1*xHDAC11
827 interaction p-values across cell types and tangles in different brain regions shown (ag: anterior gyrus, ec:
828 entorhinal cortex, hip: hippocampus, mf: medial frontal, mt: medial temporal, cg: cingulate gyrus, it: inferior
829 temporal, mes_t: mesial temporal). **(F)** An illustration of interaction effect. Individuals were stratified into three
830 groups based on the expression of *OIP5-AS1* in excitatory neurons. For each group, HDAC11 protein
831 abundance was plotted against tangle level in the hippocampus. (**G-I**) are plaque burden counterparts of (D-F).
832
833
834
835
836
837
838
839
840
841
842
843
844
845
846
847
848
849
850
851
852
853
854
855
856
857
858
859
860
861
862
863
864
865
866

Supplementary Figures

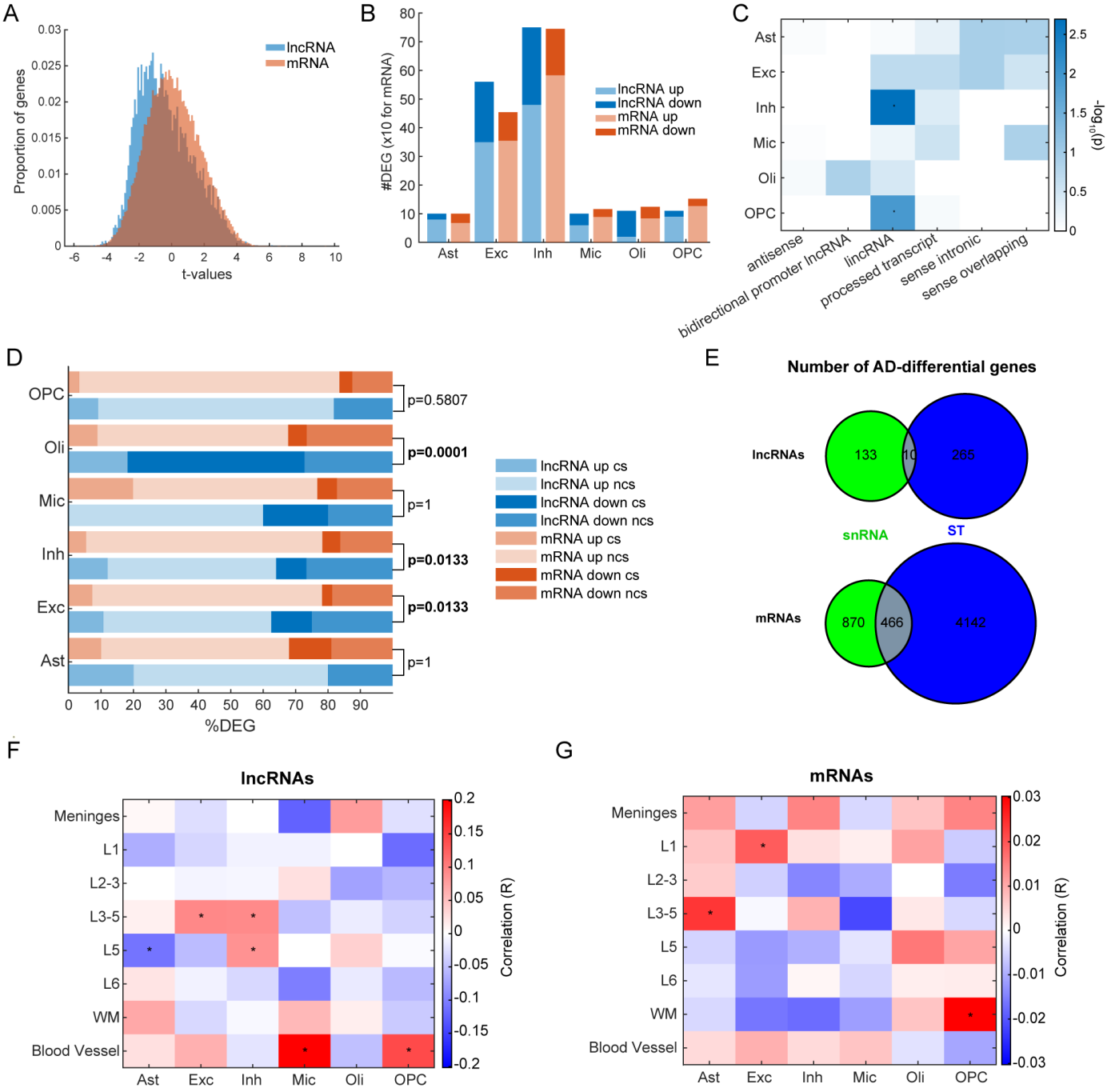

Figure S1. Differential lncRNAs and mRNAs in AD and cross-modality comparison with snRNA-seq. (**A**) Histogram showing the distribution of AD-differential t-values for mRNAs and lncRNAs. (**B**) Total numbers of AD-differential lncRNAs and mRNAs for each subregion. (**C**) Heatmap showing the enrichment of AD-differential lncRNAs for specific biotypes. (**D**) The percentage of DEGs in each snRNA cell type, split by lncRNA/mRNA, up/down in AD, and whether they are cell-type-specific (cs) or not (ncs). Fisher's exact test was applied to assess differences in cell-type-specificity between lncRNA and mRNA with p-values indicated. (**E**) Overlaps in AD-differential lncRNAs and mRNAs between ST and snRNA-seq. (**F-G**) Heatmap showing correlation (R) between subregions and cell types based on their AD differential t-values (*p<0.05) for lncRNAs (F) or mRNAs (G).

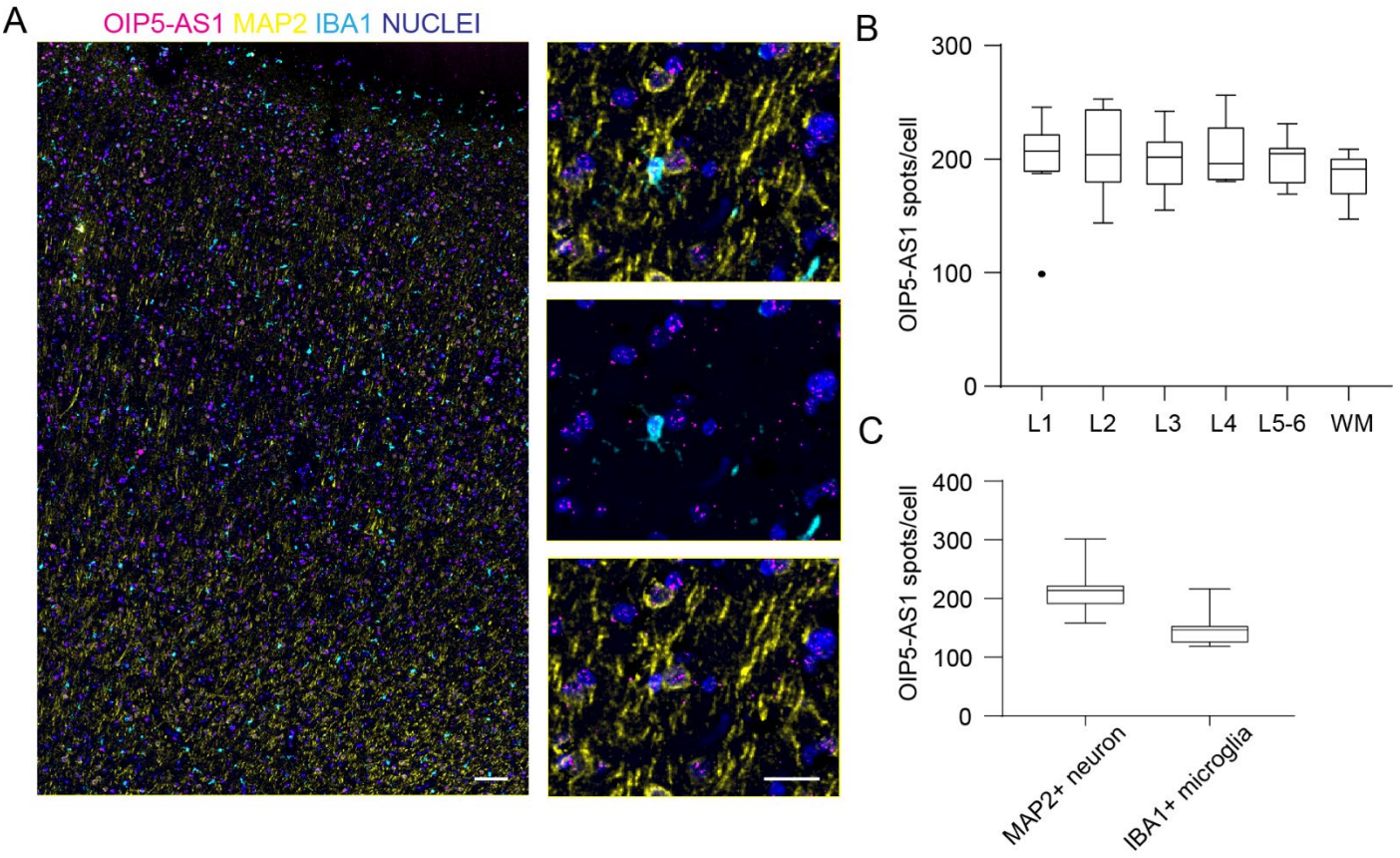

Figure S2. Validation of *OIP5-AS1* expression in human DLPFC by RNAscope.
(A) Representative RNAscope image of human DLPFC showing transcripts of *OIP5-AS1* and immunostaining for MAP2 and IBA1. Scale bars = 100 µm (overview), 20 µm (insets). (B) Boxplots of mean *OIP5-AS1* spot quantification in cortical layers, range n =103-1788 cells per layer from 8 individuals. (C) Boxplots of mean *OIP5-AS1* spot quantification by cell type, derived from a minimum of 200 MAP2+ neurons and 50 IBA1+ microglia for each of 8 individuals.

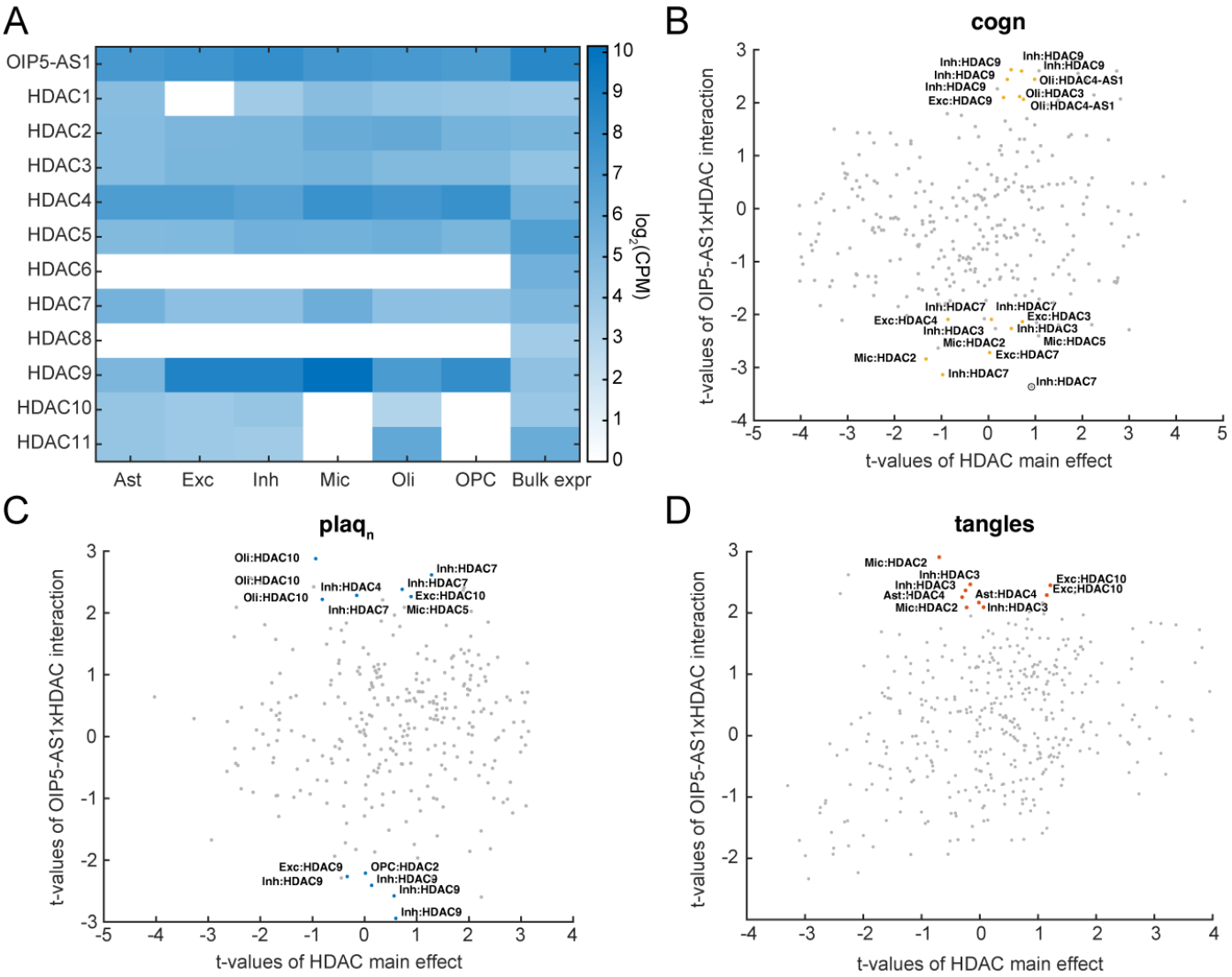

Figure S3. Association of lncRNA *OIP5-AS1* with AD phenotypes using cell-type-specific expression of HDAC RNA. (**A**) RNA expression of *OIP5-AS1* and HDAC genes in designated snRNA-seq cell types and bulk DLPFC RNA-seq. (**B-D**) Scatterplots showing t-values of the HDAC main effect (x-axis) and the *OIP5-AS1*xHDAC interaction for cognition (**B**), plaque burden (**C**), and tangles (**D**) measured in multiple brain regions. Dots are colored but not circled if interaction p<0.05 and an order of magnitude lower than the main effect p-value. The circled dot in (**B**), Inh:*HDAC7*, is the only interaction passing multiple comparison correction for the number of HDACs and cell types.

926 **Supplementary Tables**

927

928 Table S1. Subregion- and cell-type-enriched lncRNAs
929 Table S2. ST gene expression module assignments
930 Table S3. ST gene expression module preservation
931 Table S4. ST gene expression module FEA
932 Table S5. ST gene expression module AD trait associations
933 Table S6. AD-differential lncRNAs (ST, bulk, snRNA)
934 Table S7. AD-differential GSEA of ST genes
935 Table S8. AD-differential genesets including lncRNAs

936

937

938

939

940

941

942

943